47th AIAA Aerospace Sciences Meeting Including The New Horizons Forum and Aerospace Exposition
5 - 8 January 2009, Orlando, Florida

AIAA 2009-356

Size Resolved Measurements of the Reactivity of Metal Nanoparticles

Lei Zhou, Xiaofei Ma, Michael R. Zachariah*
Department of Mechanical Engineering and Department of Chemistry and Biochemistry
University of Maryland, College Park, 20742, USA

Nano-scaled metal particles have attracted interest for its potential use as a fuel in energetic materials. In this work, we combined two ion-mobility spectrometry approaches: tandem differential mobility analysis (DMA) and tandem differential mobility – particle mass analysis (DMA-APM) to study the size resolved reactivity of nickel and zinc nanoparticles. Nickel nanoparticles were generated in-situ using gas-phase thermal pyrolysis of nickel carbonyl. Four particle sizes (40, 62, 81 and 96 nm, mobility size) were then selected by using a differential mobility analyzer. These particles were sequentially oxidized in a flow reactor at various temperatures (25-1100 °C). The size and mass change of the size selected and reacted particles were then measured by a second DMA, or an APM. We found that both particle size and mass were increased as the temperature increased. However, at higher temperature (600-1100°C), a different mass and size change behavior was observed which could attribute to a phase transition between NiO and Ni_2O_3. A shrinking core model employed to extract the size- resolved kinetic parameters shows that the activation energy for oxidation decreased with decreasing particle size The burning time power dependence on particle size was found to be less than 2 and nickel particles were found to be kinetically more active than aluminum.

Zinc Nanoparticles were generated by a direct evaporation/condensation of bulk zinc, to yield single Zn-nanocrystals (NCs). In addition to studying oxidation kinetics analogous to that conducted for Ni as described above, hydrolysis kinetics are also generated. Finally and because the surface properties of NC are essentially unknown, we develop a novel method to study the evaporation kinetics of Zn NC and extract the surface energy of unsupported NCs. Direct in situ measurement of mass change using a tandem ion-mobility size and mass spectrometers is used to determine the size dependent evaporation rate. A kinetic model is used to relate the evaporation rate to the temperature dependent surface energy. We report measurements for Zn NC surface energies of 9.0 and 13.6 J/m2 at 375 °C and 350 °C, respectively. We also observed using electron microscopy the crystal edge effect which leads to an evaporation anisotropy for Zn NCs.

Corresponding author. Email:mrz@umd.edu. Phone: 301-405-4311. Fax: 301-314-9477

1

I. Introduction

Recent advancement on field of so called "nanoenergetic" materials are focused on either enhancing or tuning reactivity. On one level this issue is reduced to a length-scale argument, whereby smaller fuel/oxidizer combinations result in smaller diffusion lengths and therefore higher reactivity. On another level, this discussion leads to choices of different thermite formulation. Although there have been considerable successes in enhancing the energy release rate of thermite systems, the goal of tuning the reactivity is still a subject for further research. In one of our previous works, we reported a method to control the energy release rate of energetic nanoparticles by creation of a core shell nanostructure on the oxidizer particle.[1] Similarly, the reactivity of nanoenergetic material can also be controlled by modifying the structure of the aluminum fuel.[2] More recently we have seen that mixtures of nanoaluminum and nanoboron outperform either material on their own.[3] Those results suggest both material choices (e.g. Ni, Ti, etc.) and nanoarchitecture as means to tune the energy release profiles of materials beyond aluminum. The application of those materials would take the form of composite materials e.g. Al/Ni alloy, or metal particles with a different morphology such as aluminum core with nickel coating. While considerable opportunity exists for improvements, in actuality very little attention has been paid to the kinetics of reactivity of small metal particles beyond nanoaluminum. The reactivity of metal particles is often studied with traditional thermal analysis techniques such as TG, DTA or DSC. However, it is well known that those methods are greatly influenced by heat and mass transfer effects such that the results are biased by experimental artifacts.[4,5] Furthermore, as particle size decreases into the nano-scale, the mass transfer limitations should be reduced and we should expect to see an enhancement in reactivity. Our previous work on the oxidation of nanoaluminum particles show that both the overall rate constant and activation energy are size dependent.[4,5] Ideally, one would like to probe the intrinsic properties or reactivity of nanoparticle in a size resolved manor and conduct measurement in absence of other rate limiting kinetic effects.

In this work we employed aerosol based ion-mobility techniques to study the size resolved reactivity of metal nanoparticles. Our previous results on the study of the solid-gas phase reaction kinetics show that the reaction rate obtained using aerosol based techniques, are much higher than conventional methods, which may represent the intrinsic reactivity of nanoparticles.[4,5] The method developed here provides a generic approach for characterizing the intrinsic properties of nanoparticles. As the applications of the ion-mobility method, nickel nanoparticle oxidation kinetics and zinc nanoparticle oxidation/hydrolysis kinetics were studied using this approach.

The basic idea of the experimental approach is to prepare Ni or Zn nanoparticles of characterized size/shape (i.e. Monodisperse), and monitor size/mass changes during reaction in free-flight (i.e. no substrate). This study consists of two experiments, both of which rely on ion-mobility separation. A Tandem Differential Mobility Analyzer (DMA) system[6-8] is used to measure the size change after oxidation, while the mass change is tracked by a DMA-APM (Aerosol Particle Mass Analyzer) system.[9-12] For nickel nanoparticle oxidation, the average density obtained from mass and size measurements show the nickel nanoparticle oxidation process can be correlated to the formation of both NiO and Ni_2O_3 ($4Ni+3O_2 \rightarrow 2Ni_2O_3$, $2Ni+O_2 \rightarrow 2NiO$) and a phase change region where both the oxidation of nickel and thermal decomposition of Ni_2O_3 to NiO ($2Ni_2O_3 \rightarrow 4NiO+O_2$) occur simultaneously. The reaction rates were then extracted from the experiment data as a function of particle size. Similar to nickel oxidation study, Zn nanocrystal (NC) oxidation/hydrolysis were also investigated. Since the surface properties especially surface free energy of NC plays an essential role in nanoparticle processes such as melting, coalescence and evaporation, we also studied the evaporation kinetics of Zn NC and extract the apparent surface energy of unsupported Zn NC.
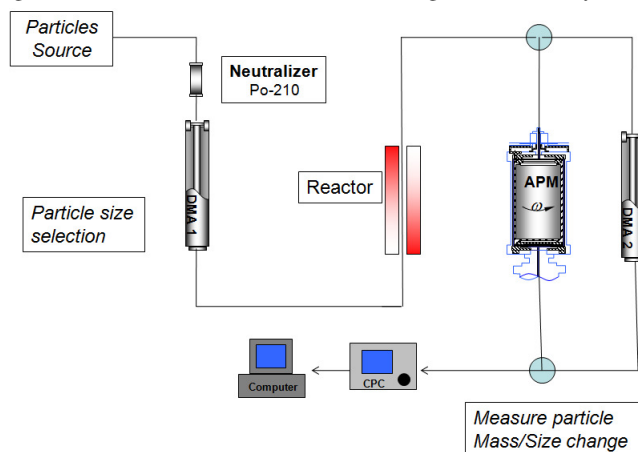
Figure 1: Schematic of ion-mobility method.

II. Experimental Approach

The experimental system consists of three components. Preparation of monodisperse nanoparticles, second, exposure of size selected particles into a controlled reaction region, and third, measurement of the size and mass

change resulting from reaction. A complete schematic of the experimental setup for probing the reactivity of metal nanoparticles using ion-mobility is shown in Fig. 1.

A. In-situ Generation of Nanoparticles

In this work, nickel or zinc nanoparticles were prepared in-situ for on-the-flight ion-mobility measurement. For the nickel oxidation kinetics study, high purity nickel nanoparticles were generated in an oxygen free environment using gas-phase thermal pyrolysis of nickel carbonyl.[13,14] Nickel carbonyl was generated in-situ by flowing of a small amount of carbon monoxide through a nickel powder bed (3 um, 99.7% Sigma Aldrich), which was placed immediately upstream of an isothermal tube reactor to thermally decompose $Ni(CO)_4$ so as to form nickel particles. Since the resulting particles are agglomerated and our experimental protocol requires individual primary particles, the generated nickel particles were size selected by the first DMA (to be described below), and subsequently heated to 1100^oC to form spherical particles. In this study, nickel nanoparticles with mobility sizes of 70, 135, 200 and 240 nm were selected using the first DMA and the size of particles shrink to a mobility size of 40, 62, 81, and 96 nm after sintering, and are thus the initial particle size before oxidation. The sintered particles were then mixed with dry air with 1:1 ratio, and enter a well characterized tube reactor for oxidation at a controlled temperature (25~1100°C).

In the study of Zn NC, evaporation/condensation was used to provide Zn NCs. Zn vapor is generated from granular Zn (purity, ≥99.99% from Sigma-Aldrich) by evaporation in a tube furnace at 550^oC with a flow of argon, and non-agglomerated Zn NCs are formed from the condensation of Zn vapor for the size-dependent oxidation, hydrolysis and surface energy study. Using the condensation/evaporation method we can produce well-defined Zn nanocrystal structures. Fig. 2 shows the SEM image of two single Zn NCs. The NCs show the shape of perfect hexagonal prism. EDS spectra obtained from the NCs in SEM confirmed that the composition is Zn. Selected Area Electron Diffraction analysis indicated that the Zn NCs have top surfaces of {0001} crystal planes and have side surfaces of $\{1\bar{1}00\}$ planes.
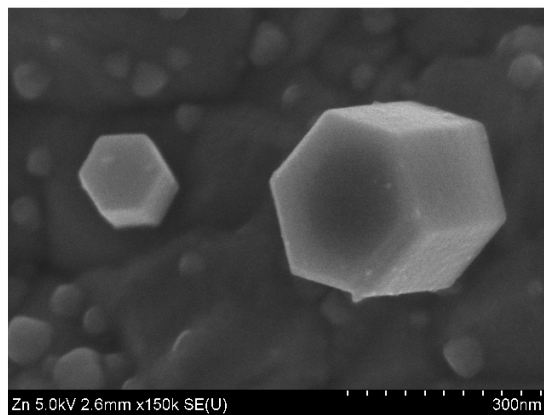
Figure 2 SEM image of the Zn nanocrystals

B. Differential Mobility Analyzer (DMA) and Aerosol Particle Mass Analyzer (APM)

The primary analytical tools employed in the experiments are a tandem differential mobility analyzer system (TDMA)[6-8,15,16] and DMA-APM (aerosol particle mass analyzer) systems.[9-12] In the experiments, particles were first charged with a Boltzmann charge distribution by exposing the aerosols to a Po-210 source, before the first DMA. The average charge state of sample particles under Boltzmann distribution is roughly neutral, with most of particles uncharged and equal amount of particles carry +/- 1 charge and +/-2 charges, etc. For example, in case of 50 nm particles, 60.2% particles will be neutral, 19.3% carry +/-1 charge, 0.6% carry +/- 2 charges, and higher charge state would be even less.[17] Considering the small percentage in the multiple charged states, we ignore multiple charged particles and assume the charged particles are all singly charged. Both the DMA and APM are configured to classify positively charge particles, and the uncertainties of the DMA/APM under current experimental conditions are estimated to be less than +/- 4 %.

The DMA consists of two concentric cylinders, which the center cylinder is held at high voltage and the outer one is on ground. The schematic of DMA is shown in Fig. 3 (a), when charged particles flow between the cylinders the electric force on the particle is balanced by the drag force, the balance of two opposite forces result a constant drifting velocity at the radial direction. The electrical mobility, Z, of a single charged particle is given by[18]

$$Z = \frac{V_r}{E} = \frac{eC_c}{3\pi\eta D_p} \qquad (1)$$

where V_r is particle radial velocity, E is the electric field, e is charge on the particle, D_p is particle diameter, η is the viscosity of carry gas and C_c is the slip correction factor given by

$$C_c = 1 + \frac{2\lambda}{D_p}\left[A_1 + A_2 \exp\frac{-A_3 D_p}{\lambda}\right] \tag{2}$$

here λ is the mean free path of the gas molecules and A_1, A_2, A_3 are constants based on experimental measurements.[18] Since the particle mobility is size dependent, particles of small size (trajectory 1) and large size (trajectory 2) have different trajectories as shown in Fig. 3 (a). At a fixed voltage, we obtain particles of same mobility size exiting the instrument (trajectory 3). As shown in Fig. 1, DMA-1 is used to selecting particles all with the same electrical mobility size and functions as a source of mono-area particles.[19] A second DMA was operated in voltage-step mode with a condensation particle counter (CPC) as a particle size distribution measurement tool to track the size change after the reaction process. A second Po-210 neutralizer was placed between the reactor, and DMA-2 to re-charge the particles. This was necessary as the high temperature treatment (sintering or high oxidation temperatures) would cause the particles to lose charge. In summary the TDMA experiment tracks changes in physical size as a result of oxidation.

In a parallel experiment the change in particle mass after oxidation was measured by an aerosol particle mass analyzer (APM) coupled with a CPC. The APM is a relatively new technique that can determine the particle mass distribution based on particle mass to charge ratio.[12] The schematic of AMP is shown in Fig. 3 (b), it consists of two

Figure 3 Schematic of (a) DMA, and (b) APM

concentric cylindrical electrodes that rotate together at a controlled speed. An electrical field is created by applying high voltage on the inner electrode while the outer one is held at ground. Single charged particles flowing within the concentric cylinders experience opposing centrifugal and electrostatic forces as shown in Fig. 3 (b) and particles exiting the instrument at fixed voltage and rotation speed all have the same nominal mass:

$$m = \frac{eE_{APM}}{r\omega^2} \tag{3}$$

Here E_{APM} is the electrical field between the two cylinders, ω is APM rotation speed and r is the distance between particle and the center of the cylinders. By scanning either the voltage or the rotation speed, the particle mass distribution (independent of particle shape) can be determined. Our previous experiments have used the DMA-APM technique to measure the inherent density of nanoparticles, as well as to study the mechanism of aluminum oxidation.[9,10]

III. Results and Discussion

A. Nickel Nanoparticle Oxidation Kinetics

Mobility size selected Ni particles of 40, 62, 81 and 96 nm (after sintering) were mixed with air and oxidized. Figure 4 (a), (b), (c) and (d) show normalized particle size distributions measured by DMA-2 at selected furnace temperatures for initial mobility size of 40, 62, 81 and 96 nm, respectively and the detailed particle peak size data are shown in table 1. The size distributions obtained for each furnace temperature were fit to a Gaussian distribution to determine the peak size. As mentioned above, the initial un-reacted particle size is determined from DMA 2 at 25°C. Further measurements of particle oxidation at 200°C show no size change, indicating that reaction if there is any is below our detection limit. The TDMA experiment indicates that the oxidation starts at ~300°C as evidenced by an increase in particle size. This size increase results are due to nickel oxidation forms a lower density oxide than the zero valent metal. However, the size increase is not continuous in temperature and in the higher temperature regions (above 600°C), a significant size decrease is observed for all particle sizes. To further investigate the nickel nanoparticle oxidation process, particle mass changes due to oxidation were tracked by the APM. Figure 5 (a), (b) (c) and (d) show the results of the APM measured mass distribution at 25°C and 700°C for initial mobility size of 40,
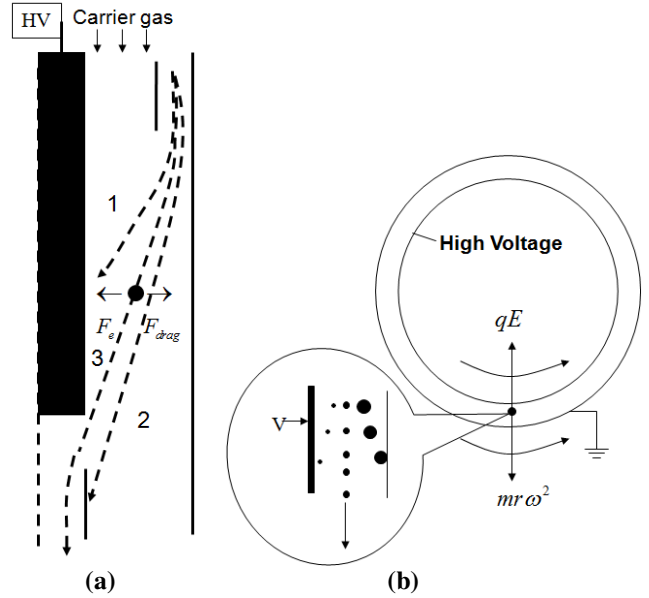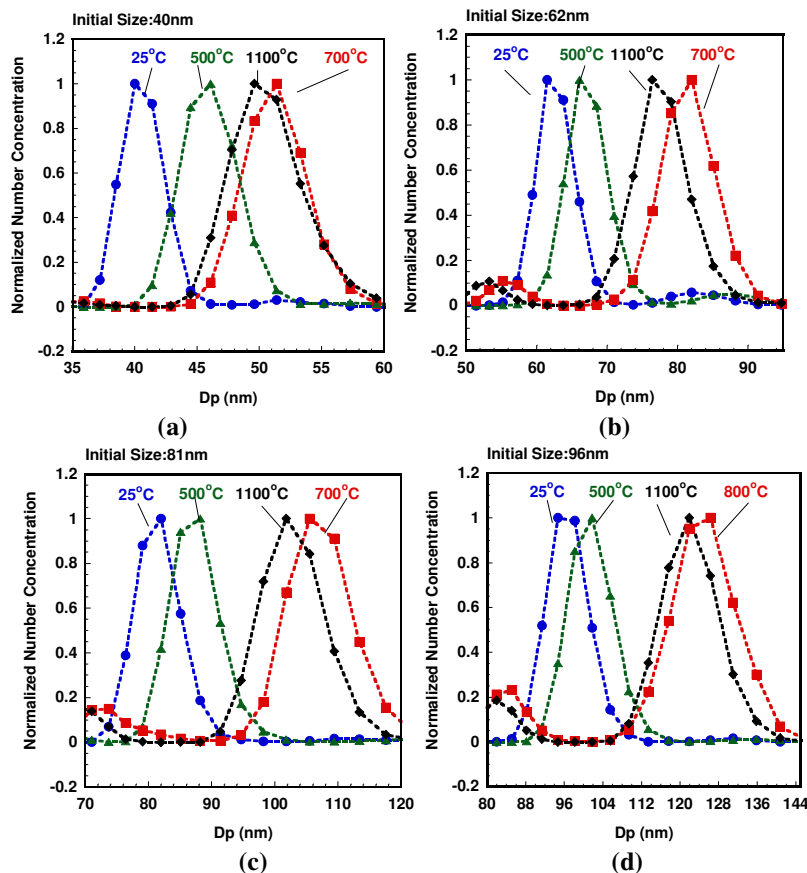
Figure 4 TDMA measured size distribution for initial size of (a) 40 nm, (b) 62 nm, (c) 81 nm, and 96 nm nickel particles at different oxidation

62, 81 and 96 nm, respectively. Because the APM has a broader transfer function compare to the DMA, especially at the low end of the APM range, a plot of the experimental data for each temperature would overlap, and would be difficult to read. For this reason, we only show the experimental results at furnace temperatures of 25°C and 700°C. The particle peak mass distribution data at each furnace temperature were fit to a Gaussian function to obtain the peak mass and are shown in table 2. It is clear from Fig. 4 and table 2 that there is a mass increase, with increasing furnace temperature, which reaches a maximum at above 600°C. On the other hand, we can see at higher temperature region, the measured value for the mass fluctuates within the experimental uncertainty for initial 40, 62, and 81 nm particles, and increases slowly with increased temperature for the initial 96 nm particle.

As we have mentioned above, nickel particles were sintered to form spherical particles before oxidation step, therefore, any size/mass change after particles pass through the oxidation furnace can be attributed solely to oxidation, e.g. not from the re-arrangement of particle morphology. The most likely explanation for our experimental observation would be the formation of an intermediate phase of the oxide, Ni_2O_3, at low temperatures, and further decomposition of Ni_2O_3 to NiO at higher temperatures. The average density profiles of reacted particles can be calculated using the TDMA and APM measured particle size and mass. We find that as the furnace temperature increases, the average density of the reacted particles decreased monotonically to 4.7-5.0 g/cm^3, consistent with the density of Ni_2O_3 (4.84 g/cm^3)[20,21]. At higher temperatures the particle density increases to 5.5-5.7 g/cm^3 and at the highest temperature investigated is roughly at a density half way between NiO (6.67 g/cm^3) and Ni_2O_3 (4.84 g/cm^3). This result suggests the oxidation to form Ni_2O_3 in the low temperature region while the process of formation of the two types of oxides, and the phase transition are coupled at higher temperatures. This is also consistent with the fact that Ni_2O_3 is the thermodynamically favorable phase at low temperature, and decomposes into NiO and oxygen at temperatures above 600°C. Presumably the particle would have a nickel core with an outer oxide layer which contains both NiO and Ni_2O_3. Both the oxidation of the nickel core and decomposition of the

5

outer Ni_2O_3 layer could occur simultaneously and result in a roughly constant particle mass as observed for small particles, and slow mass gain for large particles.
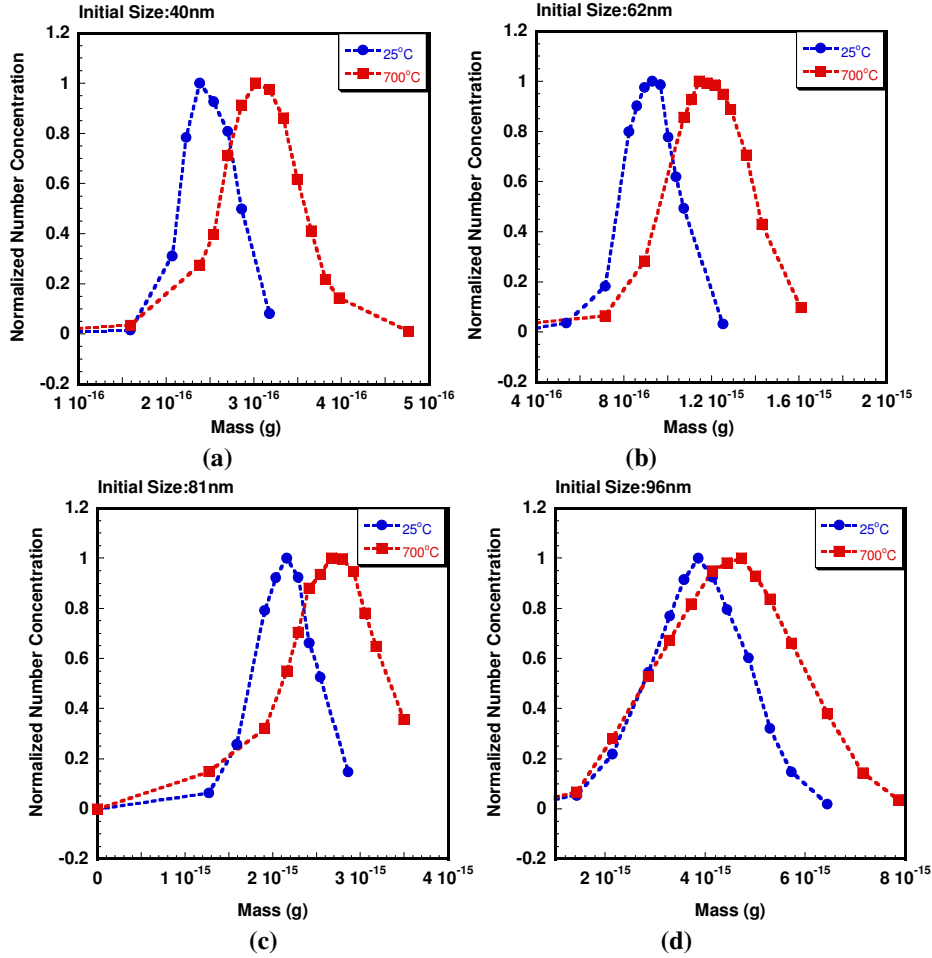
Figure 5 APM measured mass distribution for initial size of (a) 40 nm, (b) 62 nm, (c) 81 nm, and 96 nm nickel particles at different oxidation

To extract size dependent reaction kinetics, an appropriated reaction model is required. Metal oxidation theories and the transport properties of the oxides have been studied for several decades. It is believed that the diffusion of ionic vacancies and electron holes is the dominant transport process for nickel oxidation.[22] The theories proposed by Wagner for thick film growth are based on conditions of charge-neutrality, and diffusion of ions and electrons being the rate-limiting step.[23] Carter later applied the same assumptions to the shrinking core model for a spherical geometry, and derived an oxidation rate law for metal particle oxidation.[24] More recently Fromhold has developed a model focused on the oxidation rate of spherical metal particles in the low space charge limit using the coupled current approach for oxide thicknesses below 100 nm[25]. Only surface charge and linear diffusion were considered in their study, and a same rate law similar to Carter's work was obtained. This suggested to us that the diffusion controlled shrinking core model could be applied to our study as a relatively straightforward way to process our experimental results.

Following Carter's analysis at steady state, the diffusion flux through the oxide shell can be related to the reaction rate of reactant, by

$$\frac{dN_{O_2}}{dt} = -4\pi D_e C_{o_2} \frac{r_1 r_2}{r_2 - r_1} \tag{4}$$

In equation (4) r_1, r_2 are the radius of the nickel core, and the reacted particle radius. C_{o_2} is the oxygen molar concentration in gas and N_{o_2} is the moles of oxygen in oxide layer. D_e is the diffusion coefficient for ion diffusion in the oxide layer:

Table 1. Change in particle size as a function of oxidation temperature

Furnace Setting (°C)	particle size (nm)			
	40	62	81	96
25	40.0	62.0	81.0	96.6
200	40.0	62.0	81.0	96.6
300	40.2	62.5	81.3	96.9
400	41.5	63.6	81.8	97.5
500	45.9	67.0	87.1	101.2
600	51.3	77.9	95.8	110.2
700	51.2	81.4	106.9	122.7
800	50.9	81.2	106.9	124.8
900	50.1	80.7	106.5	124.7
1000	49.0	78.7	104.8	123.8
1100	50.3	77.5	102.5	121.8

Table 2. Change in particle mass as a function of oxidation temperature

Furnace Setting (°C)	particle mass ($\times 10^{-16}$g)			
	40	62	81	96
25	2.48	9.19	21.43	36.81
300	2.50	9.40	21.44	37.25
400	2.65	9.73	21.93	37.40
500	2.82	10.29	23.10	38.30
600	3.03	11.42	25.12	41.15
700	3.08	11.89	27.12	44.85
800	3.11	12.03	27.21	46.34
900	3.10	11.98	27.39	47.28
1000	3.10	11.94	27.15	47.88
1100	3.11	12.23	28.16	48.40

$$D_e = A_m \exp(-\frac{E_a}{RT}) \tag{5}$$

Here A_m is the pre-exponential factor, E_a is reaction activation energy, and R is the gas constant. Equation (4) immediately leads to the mass change rate for the reacted nickel nanoparticle, as

$$\frac{dM}{dt} = 4\pi M_{O_2} D_e C_{o_2} \frac{r_1 r_2}{r_2 - r_1} \tag{6}$$

where Mo_2 is the molecular weight of oxygen. Here we approximate the instantaneous mass changing rate $\frac{dM}{dt}$ in equation (6) with the average mass changing rate to get

$$\ln \frac{\Delta M}{\tau} = -E_a / RT + \ln(4\pi M_{O_2} C_{o_2} A_m \frac{r_1 r_2}{r_2 - r_1}) \tag{7}$$

by using the mass change measured from the APM, the average mass change rate can be calculate for each furnace temperature. The size-resolved activation energy can be obtained from an Arrhenius plot as shown in Fig. 6. Two different regions can be distinguished from the Arrhenius plot, as the oxidation process transitions to a phase change region at ~600-700°C. The kinetic parameters for both regions can be determined using linear fit. The curve fit parameter as well as the size-resolved activation energies obtained are summarized in table 3 and the results for the

low temperature region are also shown in Fig. 6. The calculated activation energies in the low temperature region decrease from 54 kJ/mol to 35 kJ/mol as the particle mobility size decreases from 96 nm to 40 nm. The activation energies are significantly lower in the phase transition region, and further investigation is needed to understand this phase behavior. The activation energy obtained here (~0.4 eV) are considerably smaller than the value of 1.5 eV reported by Karmhag et. al. for micro size Ni particles oxidation and 1.34 eV for nano size Ni particles oxidation,[26,27] and also smaller than 1.78 eV for grain boundary diffusion limited thin film oxidation reported by Atkinson.[22] This difference between conventional methods and our approach has been consistently observed in previous work.[4,5] Moreover, the activation energy obtained here are much closer to the value of 0.6~0.9 eV for electron transport in single crystal nickel oxide.[28] and consistent with the reported activation energy of 0.3 eV for single crystal Ni oxidation in the early film-thickening stage.[29] It is well known that there are significant drawbacks of the conventional methods associated with the influence of experimental artifacts.[30] In those methods, usually milligrams of bulk sample are needed, while the sample mass of our aerosol based

Figure 6 Arrhenius plots of average mass changing rate as a function of inverse temperature for nickel nanoparticle oxidation. The calculations for activation energy are only for the low temperature region.

techniques is ~ 1 fg. For a highly exothermic reaction such as metal oxidation process, the large exothermic in a bulk sample will corrupt the observed onsite temperature, and the rapid reaction will lead to heat and mass transfer effect for bulk sample. As a consequence, the kinetic parameters extracted from the conventional methods are obscured. The TDMA and DMA-APM techniques employed here allow a direct measure of mass and volume change of individual particles thus enables us to explore the intrinsic reactivity of nanoparticles with minimizing the sampling error introduced by mass and heat transfer.

Table 3. Summary for Arrhenius parameters for nickel nanoparticle oxidation

Particle Mobility Size (nm)	Temperature range (°C)	Curve fit parameters ($Y = aX + b$)		Activation energy (KJ/mol)	Effective Diffusion Coefficients (10^{-9} cm^2/s)
		a	b		
40	400~600	4216.7	-38.8	35.0 ± 0.8	0.56~4.64
62	400~600	4844.9	-36.7	40.3 ± 2.6	1.02~17.0
81	400~700	6119.4	-34.8	50.8 ± 3.0	0.27~33.7
96	400~700	6566.2	-34.1	54.6 ± 2.9	0.18~35.4
40	700~1100	1267.7	-42.2	10.5 ± 0.5	NA
62	700~1100	1336.9	-40.6	11.1 ± 1.5	NA
81	800~1100	1479.8	-39.7	12.3 ± 2.2	NA
96	800~1100	2085.3	-38.7	17.3 ± 0.4	NA

The effective diffusion coefficient is determined by calculating the unreacted nickel core radius r_1. Since the shrinking-core model used here can only count for the oxidation process, the phase transition in high temperature region will corrupt the calculation of the effective diffusion coefficient. As the consequence, the calculation is only valid in the low temperature region and the results are shown in Fig. 7. Due to the well known kinetic compensation effect, although the activation energy is considerably smaller than the value measured by the conventional offline methods , the measured diffusion coefficient are within the range of reported values.[22] Since aluminum has been

well studied and has been used extensively as a primary thermite based material, the effective diffusion coefficients for aluminum oxidation obtained from our previous work is also plotted in the figure for comparison.[4] Surprisingly to see that that nickel is actually more active than aluminum although it should be pointed out that the aluminum measurements were made with a totally different experimental approach. However despite the apparent faster kinetics of Ni, the higher enthalpy of aluminum oxide (-1675.7 kJ/mol vs. -489.5 kJ/mol for Ni_2O_3 or -239.7 kJ/mol)[20,31] implies aluminum is still a more promising energetic material that nickel. Nevertheless, Ni might find applications as an ignition source for example, or in tuning the reaction profile in mixed metal nanocomposites.

Particle burn time for different initial particle size at different temperatures was also calculated using the burn rate and the total mass change measured from the APM. These results are plotted on a log scale in Fig. 8, and show for all temperatures a diameter dependence well less than 2 ($\sim D_p^{1.4}$). For large size particles (micron size), the diffusion controlled reaction would lead to a $\sim D_p^2$ dependence,[32] and a $\sim D_p^{1.8}$ dependent is reported experimentally.[33] For nano size particles, however, a much weaker size dependent has frequently been observed.[33-35] A phenomenological model was developed for aluminum oxidation in our previous work which indicated that due to the internal pressure gradient in the particle, a $\sim D_p^{1.6}$ dependent was found.[9] More generally, for the oxidation of metal, Formhold shows that a space charge layer in the growing oxide could has significant effects on the oxidation process for particles in the range of 10 nm ~ 100 nm, which can either retard or enhance the diffusion flux through the oxidation shell depending on ionic or electronic species as rate limiting.[36,37] Our results for particle burn time suggested that a model that includes both the pressure gradient and space charge effect would be worthy of investigation.
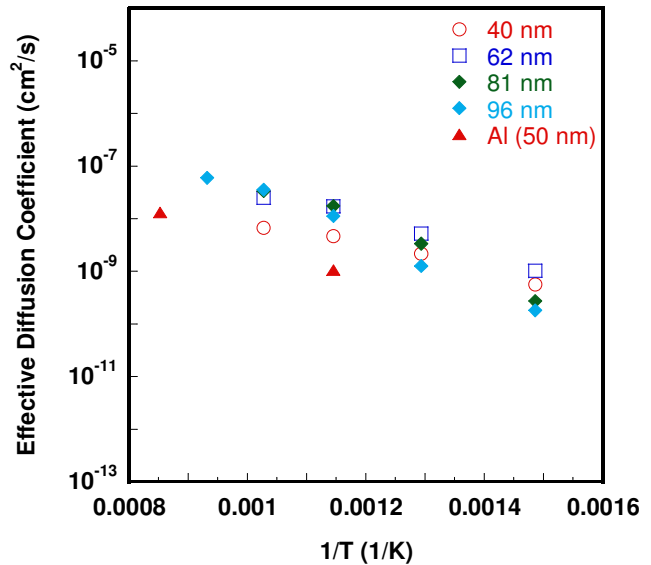
Figure 7 Arrhenius plot of effective diffusion coefficients in the low temperature region for Ni and Al.
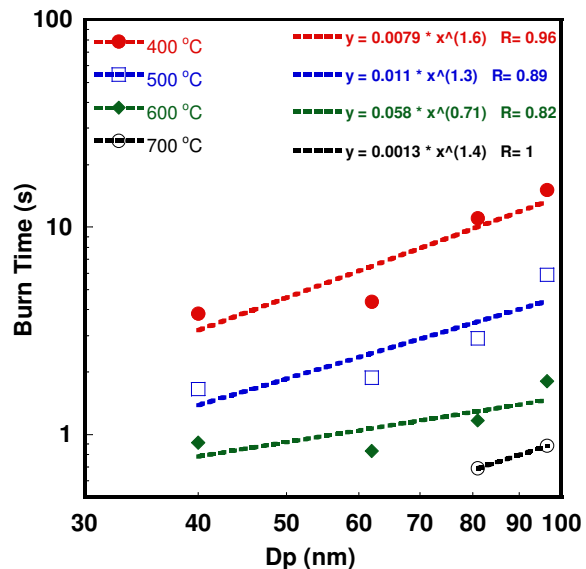
Figure 8 Nickel nanoparticle burn time at different temperatures as a function of initial particle size.

B. Zinc Nanoparticles Oxidation/hydrolysis and Surface Energy Measurement
(1) Size-Dependent Oxidation Kinetics
Zn nanoparticle oxidation kinetics study was conducted in an analogous manner to that of Ni. Zn NCs were oxidized in air in the temperature range of 200°C ~ 500°C. The peak mass at each oxidation temperature is obtained by fitting the experimental data using a Gaussian distribution. It can be noted that the peak mass of NCs remains unchanged at low temperatures, and then starts to increase due to oxidation. Based on the mass change of NCs, we can determine the percentage of conversion from Zn to ZnO at each reaction temperature. The full conversions were achieved at about 425°C, 450°C and 525°C for 50nm, 70nm and 100nm Zn NCs, respectively.

Using the kinetic model similar to the one used in the nickel oxidation study, we can exact the reaction kinetic parameters for Zn NC oxidation. The size-resolved activation energy can be obtained from an Arrhenius plot of the reaction rate as shown in Fig. 10. Two different regions of oxidation process which are represented by two joint straight lines in the plot can be distinguished for each size of Zn NCs, a slower reaction region at lower temperatures

9
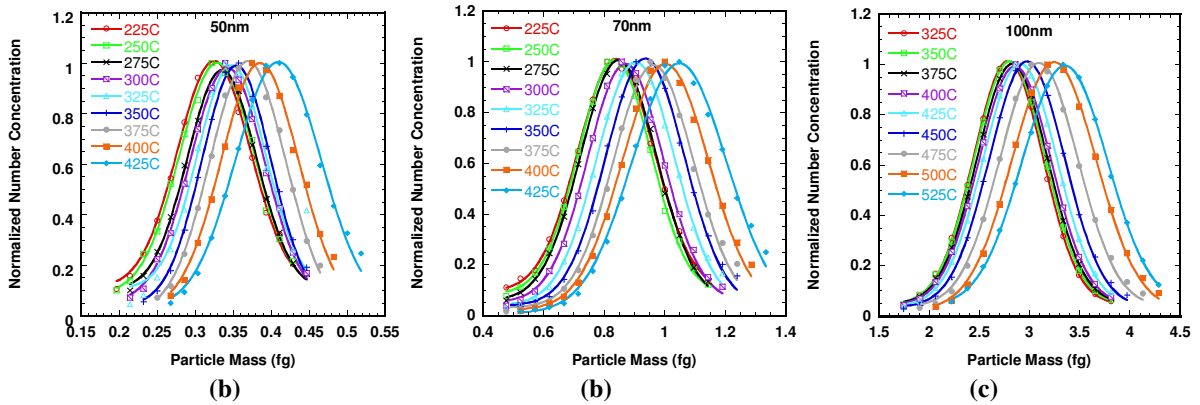
Figure 9 Normalized particle mass distributions for Zn NC oxidation at different oxidation temperatures (a) 50nm (b) 70nm (c) 100nm.
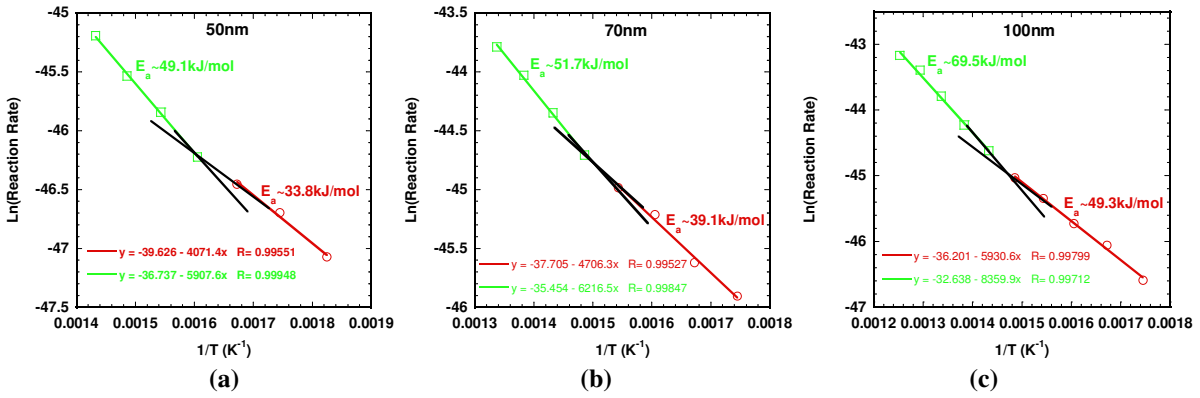
Figure 10 Arrhenius plot of reaction rate for Zn NCs oxidation (a) 50nm (b) 70nm (c) 100nm

followed by a faster oxidation region occurring at higher temperatures. The transition temperatures between the two regions are determined by finding the intersection of two straight lines. The size resolved activation energies obtained from the slope of the lines are summarized in table 4. From the experimental data we can see that with decreasing particle size, the oxidation activation energy decreased.

To further understand the two oxidation regions observed in our experiments, we collected samples of 100nm Zn NCs for electron microscopic analysis at the oxidation temperatures of 350°C, 400°C and 450°C, which are below, close to and above the transition temperature, respectively. The high resolution SEM images are shown in Fig. 11. Interesting oxidation phenomena can be observed from these pictures. From the SEM image of samples collected at 350°C (Fig. 11(a)), we can see that Zn NCs seem to have a preferable surface of oxidation during the initial stage. The Zn NCs show strong oxidation anisotropy as band-shaped oxide layers formed around the six side surfaces of the NCs while the top and bottom surfaces of NC are flat and remain unchanged. The rate of oxidation on Zn $\{1\bar{1}00\}$ planes is much faster than that on $\{0001\}$ planes. As the oxidation temperature increases to the transition temperature ~400°C, the reacted Zn NC deforms and the original hexagonal-prism shape can not be distinguished. The edges between the top surfaces and side surfaces become blurred suggest the oxidation on the top/bottom surfaces. As the oxidation temperature increases further to well above the transition temperature, the NC exhibits a flower-shaped morphology which implies that the oxides grow all around the particles. Given the fact of the observed anisotropy effect in Zn NC oxidation, it is reasonable to propose that at lower oxidation temperatures, only the side surfaces of the NCs are activated and oxide layer are formed first around those surfaces, while at higher oxidation temperatures, both the side and top surfaces are activated, which enhances the reaction rate and also requires higher activation energy.

(a)   **(b)**   **(c)**
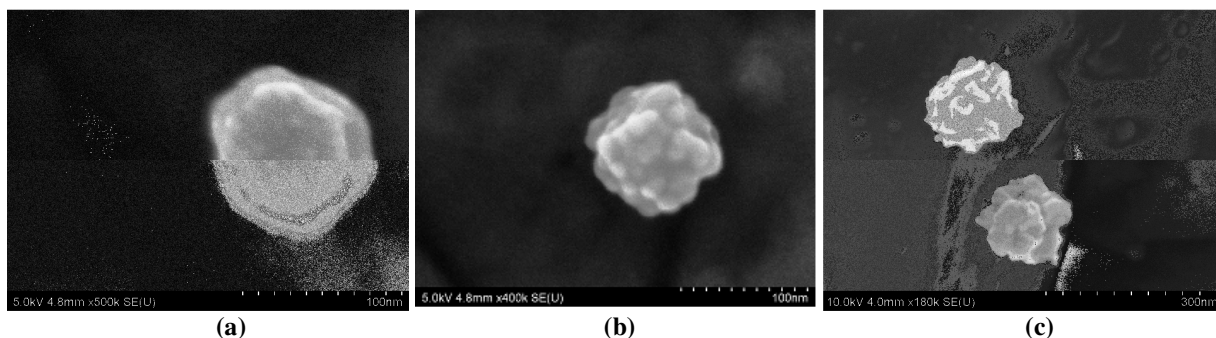
Figure 11 HR-SEM pictures of partially oxidized Zn NCs at different oxidation temperature (a) 350°C (b) 400°C (c) 450°C

Table 4. Summary of size dependent activation energy for Zn nanocrystal oxidation

Zn nanocrystal Size	Activation Energy	
	Slow Reaction Region	Fast Reaction Region
50nm	$33.8 kJ / mol$	$49.1 kJ / mol$
70nm	$39.1 kJ / mol$	$51.7 kJ / mol$
100nm	$49.3 kJ / mol$	$69.5 kJ / mol$

(a)   **(b)**
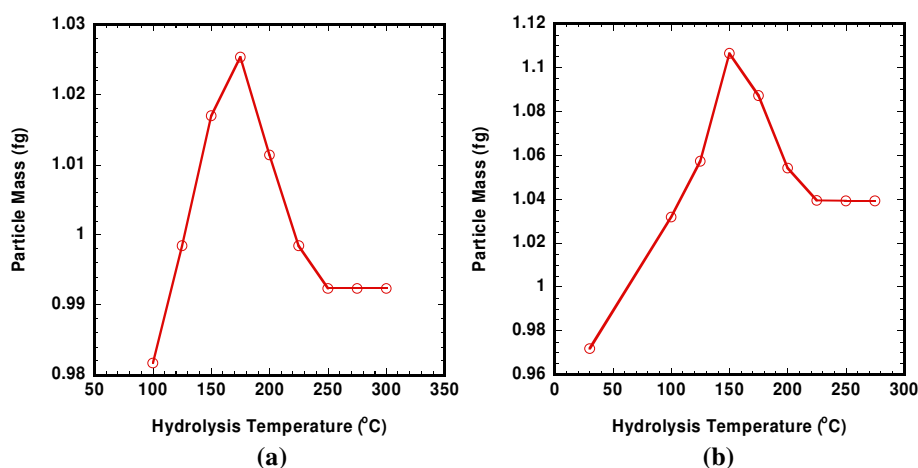
Figure 12 Mass vs. temperature for 70nm particles at different water mole concentrations (a) 3% water vapor concentration (b) 15% water vapor concentration

(3) Zn NC Hydrolysis

The setup for Zn NC hydrolysis is very similar to that of the oxidation experiment except that the mixing of clean air is replaced by the injection of water vapor. Figure 12 shows the plot of mass vs. temperature for 70nm Zn NCs at different water vapor concentrations. As we can see from the plots the mass of Zn NCs first increase with temperature, then start to decrease at the temperatures between 150°C and 175°C and finally remain unchanged at higher temperatures. A similar trend for mass change was also observed for 100nm NCs.

Based on the behavior of mass change of Zn NC during hydrolysis, we proposed the following reaction mechanism: At relatively low temperature Zn can reacts with water and generates solid zinc hydroxide and hydrogen gas. The reaction proceeds as follows:

$$Zn + 2H_2O \rightarrow Zn(OH)_2 + H_2$$
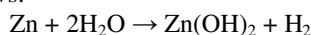
Since zinc hydroxide (Zn(OH)$_2$) has a low decomposition temperature (there is a range of reported Zn(OH)$_2$ decomposition temperature ranging from 125°C to 196°C), so when the reaction temperature is raised above the Zn(OH)$_2$ decomposition temperature, the Zn(OH)$_2$ decomposition reaction:

$$Zn(OH)_2 \rightarrow ZnO + H_2O$$
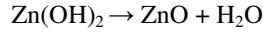
starts to compete with the hydrolysis reaction and form ZnO. Since ZnO has a smaller molecular weight than Zn(OH)$_2$, the mass of NCs starts to decrease as the temperature further increases. The above reaction mechanism is consistent with the observed trend of Zn NC mass change.
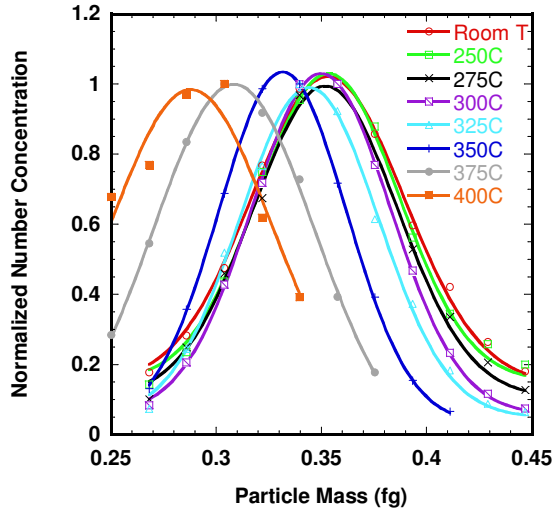
Figure 13 Normalized particle mass distributions for initial mobility particle size of 50nm NCs at different evaporation temperature.

Figure 14 SEM images of a partially evaporated 100nm Zn NCs

(4) Apparent Surface Energy of Zn NC

The surface energy is defined as the as the energy required to create a unit area of new surface. It plays an important role in nanoparticle processes such as melting, coalescence and evaporation, it also determines the equilibrium shape, faceting and crystal growth of NCs. Knowledge on surface energy can give us information of the vapor pressure over particular nanostructure surfaces, which is essential in understanding the gas-solid reaction mechanism for nano energetic materials. However, due to the obvious size issues and the interference between the NC's with its supporting environment, direct experimental measurement of surface energy for NC's has proven to be difficult

In this study we applied the ion-mobility approach to investigate the Zn NC evaporation process to extract the surface energies of unsupported NCs. A typical plot of normalized mass distributions of 50 nm Zn NCs as a function of evaporation temperature is shown in the Fig. 13. It can be noted that the peak mass of NCs remains unchanged at low temperatures, and then starts to decrease at certain critical temperature due to the evaporation.

Before we turn to interpreting the experimental ion-mobility results, it is interesting to note the anisotropy effect during the NC evaporation. This can be seen from the SEM and of a partially evaporated Zn NCs in Fig. 14. It is clearly seen that the materials tend to evaporate from the side surface of NCs first. From the SEM image, we can also observe that the edges on side surfaces etch away even further than other places. A reasonable explanation for this phenomenon is that atoms on the edges are unstable compared with the atoms on a flat surface. Once the evaporation starts, edge atoms always leave the crystal first. The evaporation of edge atoms thus helps to unzip other adjacent atoms from the crystal planes. Since the side surfaces have more edges than the top surfaces, the evaporation from the side surfaces is enhanced.

To extract surface energy, we evaluate the evaporation rate from gas kinetic theory. The particle mass change rate for a small particle (*Kn<<1*) due to evaporation is given by [18]

$$\frac{dm}{dt} = \frac{\rho \alpha S v_m (p_1 - p_d)}{(2\pi m_m k_B T)^{1/2}} \tag{8}$$

12
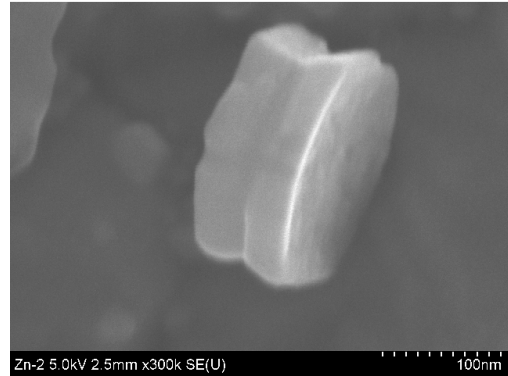
Where α is the accommodation coefficient, S is the surface area of the particle, v_m is the atomic volume of the condensing species, P_1 is the vapor pressure of the condensing species in the environment, P_d is the vapor pressure of the condensing species at the particle surface, m_m is the atomic mass of the condensing species and the k_B is the Boltzmann constant. If we assume the surface area of the NCs does not change during the initial stage of the evaporation we can convert equation (8) from a differential to an algebraic equation:

$$\Delta m = \frac{\rho \alpha S v_m (p_1 - p_d)}{(2\pi m_m k_B T)^{1/2}} \Delta t \qquad (9)$$

For crystalline particles, the vapor pressure at the NC surface can be calculated using the Kelvin equation for small crystals [38]

$$p_d = p_s \exp(\frac{2\gamma_i M}{\rho R T r_i}) \qquad (10)$$

where γ_i is the surface energy and r_i is the vector length proportional to the surface energy of each face of NC from a common origin. According to Wulff construction, the equilibrium crystal shape is determined by the information of surface energies of all crystal planes and γ_i / r_i is constant for all crystal faces. That is to say, for equilibrium NC, the partial pressure over all crystal surfaces should be the same. Since the evaporation anisotropy effect we observed, this shows the NCs we generated are not at equilibrium at first place. So the surface energy we measured from the evaporation data can be thought as an apparent surface energy of the evaporated surfaces. However this apparent surface energy can also characterize the instability of materials. The edges and side surfaces of Zn NC are relatively unstable. Since in the experiment, materials evaporate from the side surfaces only, so r_i in equation (10) is actually the vector length r normal to the side surfaces of the Zn NC measured from the center of the hexagonal prism. Based on the room temperature particle mass measurement and the c/a ratio of the synthesized NCs, we obtain the r_i corresponding to the side surfaces to be 19.8, 27.7, 40.0 and 56.8 nm corresponding to NCs of initial mobility diameters 50, 70, 100 and 150 nm, respectively. Compared with p_d, the environmental vapor pressure p_1 is essentially zero. Since when evaporation starts, materials only evaporate from the side surfaces. The surface area S in equation (9) can be approximated by $6ac$ (the total area of side surfaces). The surface energy thus calculated is for the $\{1\bar{1}00\}$ planes of Zn NC. The calculation yields an apparent surface energy $\gamma = 13.6$ J/m^2 at 350$^{\rm o}$C, and $\gamma = 9.0$ J/m^2 at 375$^{\rm o}$C for Zn $\{1\bar{1}00\}$ planes. In contrast, a surface energy of 0.993 J/m^2 has been obtained for bulk zinc by Tyson in his experiment work [39]. Vitos and his coworkers [40] applied a full charge density (FCD) linear muffin-tin orbitals (LMTO) method and calculated the surface energy of bulk Zn (0001) plane to be 0.989 J/m^2. The higher value of surface energy could be an intrinsic property of nanosized crystals. Compared with the bulk value of surface energy, our result of apparent surface energy implies that the observed vapor pressures over the NC structures are much higher than expected.

IV.   Conclusions

We applied online aerosol ion-mobility based methods to study oxidation and reactivity of nickel nanoparticles. The nickel nanoparticles were generated in-situ during the oxidation experiments using gas-phase thermal pyrolysis of nickel carbonyl. Particles of well controlled sizes and structure were generated and subsequently size selected using a DMA. The mass and size changes of reacted particles were measured using an APM and a second DMA. The experimental data can be divided into an oxidation region and a phase transit region. Based on the diffusion-controlled rate equation in the shrinking core model, we found that the activation energy of oxidation decreased from 54 kJ/mol to 35 kJ/mol as the particle size decrease from 96 nm to 40 nm at low temperatures. The absolute burning time and the effective diffusion coefficient were also determined. The same ion-mobility method was also applied to the studies of Zn NC oxidation and hydrolysis kinetics. For Zn NC oxidation, two oxidation regions have been observed and size-dependent oxidation activation energies have been extracted. For Zn NC hydrolysis study, a new low temperature Zn hydrolysis mechanism has been proposed based on the mass change of Zn NC. Finally, we applied the ion-mobility method to measure the surface energy of Zn NC. We reported measurements for Zn NC surface energies of 9.0 and 13.6 J/m2 at 375$^{\rm o}$C and 350$^{\rm o}$C, respectively. Using electron microscopy, we also observed the evaporation anisotropy and oxidation anisotropy effects for Zn NCs.

References

(1) Prakash, A.; McCormick, A. V.; Zachariah, M. R. *Nano Letters* **2005**, *5*, 1357.
(2) Park, K.; Rai, A.; Zachariah, M. R. *Journal of Nanoparticle Research* **2006**, *8*, 455.
(3) K. Sullivan; Young, G.; Zachariah, M. R. *submitted to Combustion and Flame.* **2007**.
(4) Park, K.; Lee, D.; Rai, A.; Mukherjee, D.; Zachariah, M. R. *J. Phys. Chem. B* **2005**, *109*, 7290.
(5) Mahadevan, R.; Lee, D.; Sakurai, H.; Zachariah, M. R. *J. Phys. Chem. A* **2002**, *106*, 11083.
(6) Knutson, E. O.; Whitby, K. T. *Journal of Aerosol Science* **1975**, *6*, 443.
(7) Higgins, K. J.; Jung, H. J.; Kittelson, D. B.; Roberts, J. T.; Zachariah, M. R. *Journal of Physical Chemistry A* **2002**, *106*, 96.
(8) Kim, S. H.; Fletcher, R. A.; Zachariah, M. R. *Environmental Science & Technology* **2005**, *39*, 4021.
(9) Rai, A.; Park, K.; Zhou, L.; Zachariah, M. R. *Combustion Theory and Modelling* **2006**, *10*, 843
(10) Park, K.; Kittelson, D. B.; Zachariah, M. R.; McMurry, P. H. *Journal of Nanoparticle Research* **2004**, *6*, 267.
(11) McMurry, P. H.; Wang, X.; Park, K.; Ehara, K. *Aerosol Science and Technology* **2002**, *36*, 227
(12) Ehara, K.; Hagwood, C.; Coakley, K. J. *Journal of Aerosol Science* **1996**, *27*, 217.
(13) Sahoo, Y.; He, Y.; Swihart, M. T.; Wang, S.; Luo, H.; Furlani, E. P.; Prasad, P. N. *Journal of Applied Physics* **2005**, *98*, 054308/1.
(14) He, Y. Q.; Li, X. G.; Swihart, M. T. *Chemistry of Materials* **2005**, *17*, 1017.
(15) Kim, S. H.; Zachariah, M. R. *Journal of Physical Chemistry B* **2006**, *110*, 4555.
(16) Higgins, K. J.; Jung, H. J.; Kittelson, D. B.; Roberts, J. T.; Zachariah, M. R. *Environmental Science & Technology* **2003**, *37*, 1949.
(17) Hinds, W. C. *Aerosol Technology: Properties, Behavior, and Measurement of airborne particles*, 2 ed.; John Wiley & Sons, Inc.: New York, NY, 1999.
(18) Friedlander, S. F. *Smoke, Dust, and Haze, Oxford University Press, Inc.* **2000**.
(19) Jung, H.; Kittelson, D. B.; Zachariah, M. R. *Combustion and Flame* **2005**, *142*, 276.
(20) *ICT Database of thermochemical values*; Fraunhofer Institut für Chemische Technologie:: Pfinztal, Germany, 2001.
(21) Antonsen, D. H.; Meshri, D. T. *Kirk-Othmer Encyclopedia of Chemical Technology (5th Edition)* **2006**, *17*, 106.
(22) Atkinson, A. *Reviews of Modern Physics* **1985**, *57*, 437.
(23) Wagner, C. *Z. Phys. Chem. Abt. B* **1933**, *21*.
(24) Carter, R. E. *Journal of Chemical Physics* **1961**, *34*, 2010.
(25) Fromhold, J. A. T. *Journal of Physics and Chemistry of Solids* **1988**, *49*, 1159.
(26) Karmhag, R.; Niklasson, G. A.; Nygren, M. *Journal of Applied Physics* **1999**, *85*, 1186.
(27) Karmhag, R.; Niklasson, G. A.; Nygren, M. *Journal of Applied Physics* **2001**, *89*, 3012.
(28) Aiken, J. G.; Jordan, A. G. *Journal of Physics and Chemistry of Solids* **1968**, *29*, 2153.
(29) Mitchell, D. F.; Graham, M. J. *Surface Science* **1982**, *114*, 546.
(30) Ortega, A. *International Journal of Chemical Kinetics* **2001**, *33*, 343.
(31) *CRC Handbook of Chemistry and Physics*; Hampden Data Services Ltd., 2002.
(32) Levenspiel, O. *Chemical Reaction Engineering*, 3rd ed.; John Wiley & Sons, 1999.
(33) Huang, Y.; Risha, G. A.; Yang, V.; Yetter, R. A. *Proceedings of the Combustion Institute* **2007**, *31*, 2001.
(34) Valery, I. L.; Blaine, W. A.; Steven, F. S.; Michelle, P. *Applied Physics Letters* **2006**, *89*, 071909.
(35) Young, G.; Sullivan, K.; Zachariah, M. R. "Investigation of Boron Nanoparticle Combustion"; 46th AIAA Aerospace Sciences Meeting and Exhibit AIAA-2008-0942, 2007, Reno, Nevada.
(36) A. T. Fromhold, Jr. *Theory of Metal Oxidation Volume 2*; North-Holland Publishing Company, 1980; Vol. 2.
(37) Fromhold, A. T.; Cook, E. L. *Physical Review* **1968**, *175*, 877.
(38) W.J.Dunning *General and Theoretical Introduction*; Marcel Dekker, Inc.: New York, 1969.
(39) Tyson, W. R.; Miller, W. A. *Surface Science* **1977**, *62*, 267.
(40) Vitos, L.; Ruban, A. V.; Skriver, H. L.; Kollar, J. *Surface Science* **1998**, *411*, 186.